HHS Public Access

Author manuscript

ACS Appl Mater Interfaces. Author manuscript; available in PMC 2022 September 29.

Published in final edited form as:

ACS Appl Mater Interfaces. 2021 September 29; 13(38): 45236–45243. doi:10.1021/acsami.1c11620.

Modulation of Gold Nanorod Growth via the Proteolysis of Dithiol Peptides for Enzymatic Biomarker Detection

Matthew N. Creyer, **Zhicheng Jin**, **Colman Moore**
Department of Nanoengineering, University of California, San Diego, California 92093, United States;

Wonjun Yim,
Materials Science and Engineering Program, University of California, San Diego, California 92093, United States;

Jiajing Zhou,
Department of Nanoengineering, University of California, San Diego, California 92093, United States;

Jesse V. Jokerst
Department of Nanoengineering, Materials Science and Engineering Program, and Department of Radiology, University of California, San Diego, California 92093, United States;

Abstract

Gold nanorods possess optical properties that are tunable and highly sensitive to variations in their aspect ratio (length/width). Therefore, the development of a sensing platform where the gold nanorod morphology (i.e., aspect ratio) is modulated in response to an analyte holds promise in achieving ultralow detection limits. Here, we use a dithiol peptide as an enzyme substrate during nanorod growth. The sensing mechanism is enabled by the substrate design, where the dithiol peptide contains an enzyme cleavage site in-between cysteine amino acids. When cleaved, the peptide dramatically impacts gold nanorod growth and the resulting optical properties. We demonstrate that the optical response can be correlated with enzyme concentration and achieve a 45 pM limit of detection. Furthermore, we extend this sensing platform to colorimetrically detect tumor-associated inhibitors in a biologically relevant medium. Overall, these results present a subnanomolar method to detect proteases that are critical biomarkers found in cancers, infectious diseases, and inflammatory disorders.

Graphical Abstract

Corresponding Author: **Jesse V. Jokerst** – Department of Nanoengineering, Materials Science and Engineering Program, and Department of Radiology, University of California, San Diego, California 92093, United States; jjokerst@ucsd.edu.

Supporting Information

The Supporting Information is available free of charge at https://pubs.acs.org/doi/10.1021/acsami.1c11620.
GCKGCG structure, sensing schematic, temperature-dependent proteolysis, GCKGCG cleavage, low GCKGCG concentration, trypsin control, TEM images, HR-TEM image of AuNR, HR-TEM image of AuNP, Au–S binding, control peptide structures, GGKGCG cleavage, 18 h growth, interference experiment, images of control, images demonstrating detection, schematic of temporal cleavage, temporal color change, TEM images, BPTI control, and LOD calculation (PDF)

Complete contact information is available at: https://pubs.acs.org/10.1021/acsami.1c11620

The authors declare no competing financial interest.

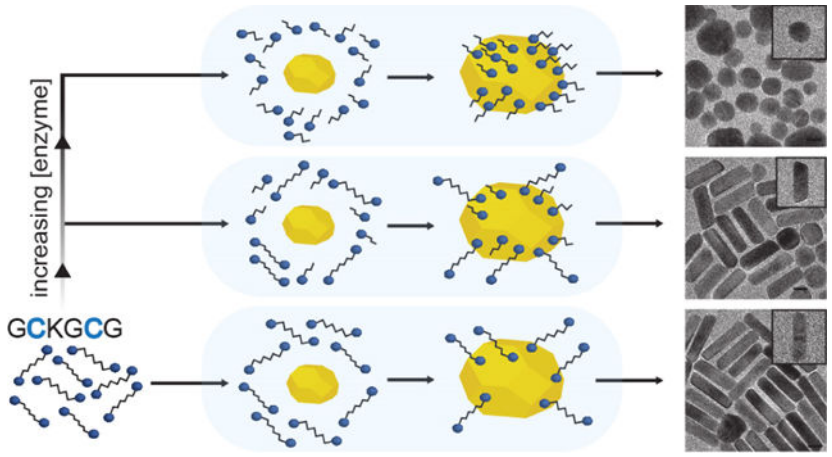

Keywords

proteolysis; enzyme activity; peptides; biosensing; gold nanorods; biomarkers

INTRODUCTION

Plasmonic gold nanomaterials have attracted immense research attention and are found in a variety of applications such as biomedical imaging,[1–4] drug delivery,[5,6] theranostics,[7,8] and biosensing.[9–11] They are extremely useful in sensing due to their large surface-area-to-volume ratio that enables substantial ligand loading and thus sensitivity.[12] Furthermore, they possess remarkable optical properties that are tunable based on the size and aggregation state. In particular, spherical gold nanoparticles (AuNSs) that exhibit a localized surface plasmon resonance (LSPR) and a correspondingly large scattering cross section in the visible region have been utilized in colorimetric assays to detect an array of biomarkers.[13]

Unlike AuNSs, anisotropic gold nanostructures possess optical properties that are tunable via more nuanced structural changes such as edge sharpness in gold nanocubes,[14] tip sharpening or dulling in gold nanostars,[15] and possibly the most reported alterations in the aspect ratio of gold nanorods (AuNRs).[16–19] Aspect ratio-dependent optical properties are especially pronounced in AuNRs because they exhibit both a transverse and longitudinal LSPR located along their short and long axis, respectively. The longitudinal plasmon has been extensively studied because it has a substantially larger molar absorptivity than comparatively sized AuNSs while having a peak extinction in the near-infrared (NIR) region.[20]

Numerous methods have been developed to tune the optical properties and aspect ratio of AuNRs.[21] The simplest techniques involve adjustments to the ratio of reactants, where higher Ag(I) concentrations result in higher aspect ratios and lower ascorbic acid and seed concentrations result in lower aspect ratios.[22,23] Changing from ascorbic acid to more mild reducing agents and the addition of aromatic weak acids such as salicylate and hydroquinone can produce high-aspect-ratio rods with less spherical impurities.[24–26] Other methods, and of most relevance to this study, include the addition of thiolated biomolecules that form

Au–S bonds on particular crystal facets altering the gold deposition rate and nanoparticle growth trajectory. The addition of thiol-containing bioadditives glutathione (GSH), cysteine (Cys), and methionine into a AuNR growth solution was recently demonstrated to be a reliable method to reduce their aspect ratio.[27] Postsynthesis modifications have also been employed, where ligand sizes ranging from small thiolated molecules (e.g., GSH, Cys, and thiocholine) to large biomolecules such as DNA and bovine serum albumin have been shown to impact the overgrowth of AuNRs.[28]

Published work on the modulation of AuNR growth in the presence of proteolysis is rare. Liz-Marzán and coworkers showed that acetylcholinesterase can hydrolyze acetylthiocholine to produce the thiol-containing molecule thiocholine which then binds to AuNRs during growth.[29] Other reports typically involve nanorod overgrowth or H_2O_2 etching where the aspect ratio is tuned via Fenton-like reactions.[30–34] This approach proved to be a reliable method to colorimetrically detect cancer biomarkers in the urine of bladder cancer patients.[35] Despite these advances, a nanoparticle-based sensing mechanism where the aspect ratio of synthesized AuNRs (and resultant optical properties) is modulated in the presence of cancer biomarkers is yet to be demonstrated.

Here, we use a gold nanoparticle-peptide sensor that utilizes the differential in adsorption between a parent peptide and its cleaved counterpart to modulate gold nanorod synthesis in response to trypsin activity. We use trypsin as a model enzyme because it is found at elevated concentrations in the serum and urine of acute pancreatitis and cancer patients (0.06–3.6 μM)—especially pancreatic cancer patients—and predictably cleaves after Lys and Arg amino acids.[36,37] We demonstrate that trypsin in conjunction with the dithiol peptide Gly-Cys-Lys-Gly-Cys-Gly (GCKGCG) can alter AuNR growth to produce a final mixture of high-aspect-ratio rods, low-aspect-ratio rods, and faceted nanospheres. The relative ratio of these products greatly impacts the optical properties of the solution and can be correlated with enzyme activity. To investigate this sensing mechanism, we test a series of control peptides and show that the key for nanoparticle shape modulation is the number and location of Cys amino acids within the peptide substrate. The time-to-readout, the temporal cleavage of GCKGCG by trypsin, and the inhibition of trypsin by tumor-associated inhibitors are also presented and analyzed within the context of our platform.

EXPERIMENTAL SECTION

Materials.

Gold(III) chloride trihydrate, cetyltrimethylammonium bromide (CTAB), hydroquinone, sodium borohydride, silver nitrate, trifluoroacetic acid (TFA), 2,2′-(ethylenedioxy)diethanethiol, thioanisole (EODT), anisole, piperidine, trypsin from porcine pancreas (T4799), and bovine pancreatic trypsin inhibitor (BPTI) were purchased from Sigma-Aldrich. Fmoc-amino acids, Fmoc-Gly-Wang resin, and HBTU were received from Aapptec (Louisville, KY, USA). Diisopropylethylamine and ethyl ether anhydrous were purchased from Fisher Scientific. GCKGCG, GGKGGG, and GGKGCG were either purchased from Genscript Inc. (New Jersey, USA) or synthesized. Pooled human urine was collected from Innovative research (Novi, MI).

Characterization.

Transmission electron microscopy (TEM) images were collected using a Thermo Fisher Talos F200X G2 operating at 200 kV and analyzed using ImageJ software. Extinction spectra were collected using a Perkin Elmer Lambda 1050 UV–vis–NIR spectrometer. High-performance liquid chromatography was performed using a Shimadzu LC-40 and a 5 μm C18 column (20 × 100 mm).

Synthesis of Peptides.

GCKGCG, GGKGGG, and GGKGCG were made using standard Fmoc synthesis on an Aapptec eclipse personal peptide synthesizer. Wang resin was used as the solid support for all peptides and was cleaved using a mixture of TFA/EODT/thioanisole/anisole (88:5:5:2, v/v) for 3 h under an argon blanket. The freshly cleaved peptide was precipitated in −80 °C diethyl ether and washed several times (3×) using centrifugation. After the final centrifugation cycle, diethyl ether was decanted and the white peptide slurry was dissolved in an H_2O/glacial acetic acid mixture (90:10, v/v) to ensure TFA salt replacement with acetate salt during lyophilization. The peptide was frozen, lyophilized overnight, and then stored at −20 °C under an argon blanket.

Purification of Peptides.

The peptides were dissolved in a mixture of water and acetonitrile at 4 mg/mL and applied to the column through a 1 mL loop. The sample was eluted at 1 mL/min with a 30 min gradient from 10 to 40% solvent B, where solvent A is water (0.05% TFA solution) and solvent B is acetonitrile (0.05% TFA solution). Preparative injections were monitored at 190, 220, and 254 nm. The purified peptide was frozen at −80 °C and lyophilized overnight to produce a white powder. Chemical structures of peptides were confirmed using electrospray ionization–mass spectrometry (ESI–MS).

Seed Synthesis.

Seed-mediated growth was employed with slight modification. CTAB (5 mL, 0.2 M) and $HAuCl_4 \cdot 3H_2O$ (5 mL, 0.5 mM) were mixed under mild stirring at 30 °C and held for 5 min to ensure full complexation between gold salt and CTAB.[38] $NaBH_4$ (600 μL, 10 mM) was injected under vigorous stirring, leading to a light brown solution.

Peptide-Protease-Mediated AuNR Growth.

Peptide and trypsin were incubated at 37 °C at the desired concentrations for 1 h in phosphate-buffered saline (PBS) buffer (137 mM NaCl, 10 mM Na_2HPO_4, 2.7 mM KCl, 1.8 mM KH_2PO_4, pH 7.4). The growth solution was prepared with slight modification as described elsewhere by adding $HAuCl_4$ (2.5 mL, 1.0 mM) and $AgNO_3$ (30 μL, 0.1 M) to CTAB (2.5 mL, 0.5 M) in a 20 mL scintillation vial under mild stirring. Next, hydroquinone (162 μL, 0.1 M) was injected into the solution causing a color change from orange to transparent. Next, 53 μL of the peptide and trypsin mixture was added to the growth solution to give the final reported concentrations and mixed for 30 s. Last, 80 μL of the seed solution was stirred in the growth solution for 30 s, and the reaction mixture was incubated for 15 h in a 30 °C water bath. Nanoparticle samples were purified by centrifugation at 12,000*g* and

redispersed to their original volumes. Experimental procedures for purely peptide-mediated AuNR growth were identical to samples mentioned above but in the absence of trypsin.

Inhibition Experiment.

Trypsin, BPTI, and GCKGCG were all dissolved in a 1:1 mixture of PBS and pooled human urine. The protease, inhibitor, and peptide mixture were incubated for 1 h at 37 °C prior to injection (53 μL) into the growth solution containing CTAB (2.5 mL, 0.5 M), $HAuCl_4$ (2.5 mL, 1.0 mM), $AgNO_3$ (30 μL, 0.1 M), and hydroquinone (162 μL, 0.1 M) to give concentrations of 500 pM, 5.0 nM, and 1.0 μM. 80 μL of the seed solution was added to the growth mixture and stirred for 30 s. The reaction mixture was incubated for 18 h in a 30 °C water bath before characterization. Experiments were performed in triplicate on different days from different stock and seed solutions.

RESULTS AND DISCUSSION

We used the peptide GCKGCG that has two Cys (C) located on either side of the Lys (K) protease cleavage site to differentially modulate AuNR growth in the presence of trypsin (Figure 1A). GCKGCG and trypsin were incubated prior to addition into the AuNR growth solution (Figure 1B) which contained CTAB, $HAuCl_4$, $AgNO_3$, and hydroquinone; the reaction was initiated upon injection of the gold nanoparticle seed (Scheme S1). A seed-based protocol was employed to supply a Au(0) surface for thiols to bind and modify nanoparticle growth (Figure 1C), and we used hydroquinone instead of ascorbic acid as a reductant because it minimizes spherical impurities and produces rods with a large, highly tunable optical window.[39] Successful trypsin detection is achieved because substrate cleavage results in the production of two monothiol peptides that bind to the gold surfaces and redirect AuNR growth (Figure 1D).

Increasing amounts of GCKGCG were added into the AuNR growth solution to study the relationship between peptide concentration and the longitudinal LSPR (Figure 2A). When no peptide was injected, the LSPR remained in the NIR range (~1100 nm) as expected. With increasing peptide concentrations, the longitudinal peak gradually blue-shifted from 1098 to 784 nm, and the extinction intensity decreased from 1.8 to 0.93, indicating a reduction in both the AuNR aspect ratio and yield.[40] Furthermore, the transverse LSPR at 506 nm became progressively obscured due to the scattering of AuNS impurities with diameters of 20–40 nm.[41] The morphological dependence of AuNRs to peptide concentration is caused by the cysteine thiols that disrupt the surface energy between the gold seed and CTAB. During standard preparations of AuNRs (ones that lack thiol additives), anisotropic growth occurs as a result of the preferential growth of {111} over {110} facets due to their differences in surface energy and adsorbed CTAB.[42,43] Anisotropic growth is attenuated upon the inclusion of GCKGCG or cleaved products because the Au–S bond is more energetically favorable than the adsorption of CTAB molecules and causes nonspecific Au(I) deposition and hence spherical impurities.[44,45]

We exploited this phenomenon by using the difference in amino-acid-directed gold nanoparticle growth between the parent peptide before (GCKGCG) and after cleavage (GCK + GCG) to detect the cancer biomarker trypsin. Figure 2B shows gold nanoparticles made

with 1.0 μM GCKGCG and varying amounts of trypsin incubated for 1 h at 37 °C prior to injection into the growth solution (Figure S2). Proteolytic cleavage of GCKGCG at the Lys amino acid was confirmed using high-performance liquid chromatography and ESI–MS (Figure S3). Without trypsin, the longitudinal LSPR showed a maximum extinction at 841 nm. Increasing the amount of trypsin caused the longitudinal LSPR (Ex_L) to blue-shift and decrease in intensity; total scattering at 550 nm (Ex_{550nm}) was increased due to the greater percentage of spherical impurities. We generated a response curve by taking the ratio of Ex_{550nm} to Ex_L and plotting it against trypsin concentration. An LOD of 45 pM was calculated based on the methods described by Armbruster and Pry (Figure 2C).[46] At a trypsin concentration of 150 pM, the absorbance and scattering characteristics of the solution changed enough as to be detectable by eyes (Figure 2D). We chose 1.0 μM GCKGCG to maximize the change in LSPR and allow colorimetric detection, as lower concentrations of peptide gave a weaker optical shift even at a high trypsin concentration (Figure S4). To verify that detection was caused by the cleavage of GCKGCG and not trypsin interfacing with the gold surface or interfering with CTAB micellization during growth,[47] we performed control syntheses and confirmed that trypsin alone cannot change the nanorod growth process (Figure S5).

Figure 2E contains TEM images that show the shape evolution of gold nanoparticles with various trypsin concentrations, while GCKGCG is maintained at 1.0 μM. With no trypsin added during the incubation step, the AuNR yield was 77 ± 2.3% with an aspect ratio of 4.9 ± 0.28. Further increases in the amount of trypsin lead to the synthesis of lower-aspect-ratio AuNRs and in lower yields. Low-magnification TEM images and AuNR yields can be found in Figure S6. No AuNRs were formed at the highest trypsin concentration of 500 pM.

To investigate how the proteolysis of GCKGCG by trypsin impacts the final particle morphology, we collected high-resolution TEM (HR-TEM) images and fast Fourier-transform (FFT) patterns from samples prepared without and with trypsin. AuNRs made with no trypsin had FFTs with reflections indexed to the {100} and {110} Au crystal planes, confirming their single crystallinity (Figure S7). This is in agreement with the crystalline structure of CTAB—AuNRs previously reported.[48] In comparison, nanoparticles made with the highest trypsin concentration contained polycrystalline impurities and had FFTs that lacked an indexable diffraction pattern. HR-TEM imaging also confirmed the synthesis of multiply twinned gold nanostructures (Figure S8).[49] This morphological dependence on trypsin concentration is presumably caused by the increase of monothiolated peptides upon substrate cleavage, which bind to the lower-index Au crystal planes that would typically evolve into rod tips during growth. Au–S bond formation and Au(I) reduction both occur simultaneously after seed injection, although complete Au–S binding occurs in less than 5 min, while complete gold reduction takes ~3 h (Figure S9). This causes Au deposition on the seed surface to be redirected from the low-index planes and leads to the synthesis of faceted gold nanospheres.[50]

To confirm the proposed mechanism, we synthesized (Figure S10) and tested two control probes: GGKGGG containing no thiol and GGKGCG containing a single thiol near its C-terminus end. GGKGGG was tested to reaffirm that the nanoparticle morphology was modulated via Au–S bonds and not through carboxylate or amino groups.[51–53] Indeed, 1.0

μM GGKGGG and increasing trypsin concentrations did not alter the AuNR growth process (Figure 3A). Although the carboxylate and amino groups likely play a role in Au(I) surface reduction during growth, the above findings indicate that Au–S bonds have the most impact on the final nanoparticle morphology. GGKGCG contains a single thiol and blue-shifts the longitudinal LSPR with increasing concentration in a similar manner to GCKGCG (Figure 3B). When 1.0 μM GGKGCG and increasing amounts of trypsin were incubated before injection into the growth solution, though, no blue shift or reduction in the intensity of the longitudinal LSPR was observed (Figure 3C). We attribute the failure of GGKGCG to act as a trypsin sensor due to its monothiol nature, where cleavage at the Lys amino acid (Figure S11) does not increase free thiol species that can bind to the gold surface during growth as is the case with GCKGCG.

After investigating the sensing mechanism, we sought to determine the time-to-readout and the nanoparticle growth process by monitoring the LSPRs after seed injection for 4 h in 15 min intervals. Figure 4A shows the time evolution of nanoparticles prepared with 1.0 μM GCKGCG and 0 pM trypsin. The longitudinal LSPR maximum first appears around 771 nm (1 h after the injection of the seed). Over the next 1 h, the intensity of the LSPR maximum increases as well as red-shifts to 908 nm before blue-shifting to 863 nm in the final 2 h. A final UV–vis spectrum was attained after 18 h that shows a final LSPR maximum of 828 nm (Figure S12). This optical behavior is consistent in standard AuNR syntheses where initial seed-symmetry breaking results in high-aspect-ratio rods that then grow widthwise from adatom addition to the boundary between {111} and {100}/{110} crystal planes.[54]

Figure 4B shows the time evolution of nanoparticles prepared with 1.0 μM GCKGCG and 500 pM trypsin. After 30 min, the initial LSPR at 536 nm with an extinction of 0.023 gradually develops over 3.5 h to have a final LSPR of 542 nm with an extinction of 1.03. This optical behavior is akin to rods prepared in the presence of GSH—a biologically abundant tripeptide that also contains a cysteine amino acid.[55] Additionally, the absence of an extinction increase at wavelengths >850 nm indicates that no high-aspect-ratio nanoparticles were synthesized. To the naked eye, the growth solutions that contained no trypsin and trypsin both showed color ~30 min (Figures S14 and 15), although it was difficult to discern a difference between them until 1 h postseed injection (Figure 4, insets). Including the 1 h incubation period before growth, these experiments show that the visual time-to-readout of our test is ~2 h.

To demonstrate the ability of our system to monitor the temporal cleavage of our substrate, we performed experiments with a constant GCKGCG and trypsin concentration and increasing incubation times (Scheme S2). Aliquots of the peptide and trypsin mixture were taken from the same stock, and nanoparticles were synthesized from the same seed to control for variation between growth solutions. Figure 4C shows a reduction in intensity of the longitudinal plasmon mode from 1.47, 1.14, 1.01, 0.81, 0.48, and 0.28 for incubation times of 0, 5, 10, 20, 40, and 60 min, respectively. Taking the ratio of Ex_{550nm} to Ex_{L} and plotting it against their incubation times give a curve that mirrors a pseudo-first order enzymatic kinetic curve. This accords with conventional fluorogenic substrates that similarly probe enzymatic activity.[56–58] The increased scattering at 550 nm is visible by eyes (Figure S16) and caused by an increase in the number of spherical impurities synthesized (Figure

4D). AuNR yields and TEM images at all incubation times are provided in Figure S17. Taken together, this once again confirms that the shape and ratio of final nanoparticles are determined by the amount of substrate converted to the product by trypsin and serves as a valuable proxy to probe proteolysis.

Pancreatic secretory trypsin inhibitors are tumor biomarkers first identified in the urine of patients with ovarian cancer.[59] Later studies confirmed that enhanced levels are also found in gynecological, pancreatic, and gastrointestinal cancers.[60–62] As a proof-of-concept, we incubated GCKGCG, trypsin, and BPTI in a 1:1 mixture of pooled human urine and PBS. Figure 5A shows a significant blue shift in the longitudinal LSPR in the absence of BPTI (−) and no LSPR shift with BPTI (+). The BPTI (+) curve produces a response as if no trypsin was added during incubation, signifying successful inhibition and minimal cleavage of the peptide substrate. Control experiments were performed where the LSPR exhibited no dependence on BPTI in the absence of trypsin (Figure S18). Additionally, the difference in the ratio of the longitudinal plasmon resonance and the extinction at 550 nm for both BPTI (−) and BPTI (+) is statistically significant (** $p < 0.01$). The colorimetric LOD is 5 nM, and the color difference is easily observed (Figure 5B). These experiments demonstrate that this approach enables the colorimetric detection of inhibitors associated with tumor progression in a biologically relevant fluid.

CONCLUSIONS

Observing the optical and morphological difference between AuNRs grown with uncleaved and cleaved dithiol peptides is a powerful tool to monitor enzyme activity. We demonstrated that this response is colorimetric and caused by an increase in free thiol species upon proteolysis. More specifically, we elucidated the sensing mechanism which is enabled by a peptide that contains an enzyme cleavage site sandwiched between two cysteine amino acids. As a proof-of-concept, we showed that this sensing mechanism could be extended to discriminate between urine samples containing tumor-associated inhibitors by the naked eye. Further directions include the use of more complex peptides with multiple cleavage and Cys sites, utilization of other anisotropic gold nanoparticles (e.g., nanocubes, nanoprisms, and so forth), and computationally driven studies that could inform more robust peptide designs.

Supplementary Material

Refer to Web version on PubMed Central for supplementary material.

ACKNOWLEDGMENTS

The authors acknowledge NIH funding under R01 DE031114. MNC acknowledges fellowship support from NIH T32 CA153915. CAM acknowledges support from ARCS (Achievement Reward for College Scientists) and the National Science Foundation Graduate Research Fellowship Program under grant no. DGE-1650112.

REFERENCES

(1). Mantri Y; Jokerst JV Engineering Plasmonic Nanoparticles for Enhanced Photoacoustic Imaging. ACS Nano 2020, 14, 9408–9422. [PubMed: 32806027]

(2). Yim W; Zhou J; Mantri Y; Creyer MN; Moore CA; Jokerst JV Gold Nanorod–Melanin Hybrids for Enhanced and Prolonged Photoacoustic Imaging in the Near-Infrared-II Window. ACS Appl. Mater. Interfaces 2021, 13, 14974–14984. [PubMed: 33761255]

(3). Jokerst JV; Cole AJ; Van de Sompel D; Gambhir SS Gold Nanorods for Ovarian Cancer Detection with Photoacoustic Imaging and Resection Guidance via Raman Imaging in Living Mice. ACS Nano 2012, 6, 10366–10377. [PubMed: 23101432]

(4). Chen F; Si P; de la Zerda A; Jokerst JV; Myung D Gold Nanoparticles to Enhance Ophthalmic Imaging. Biomater. Sci 2021, 9, 367–390. [PubMed: 33057463]

(5). Cheng Y; Samia AC; Meyers JD; Panagopoulos I; Fei B; Burda C Highly efficient drug delivery with gold nanoparticle vectors for in vivo photodynamic therapy of cancer. J. Am. Chem. Soc 2008, 130, 10643–10647. [PubMed: 18642918]

(6). Chen F; Hableel G; Zhao ER; Jokerst JV Multifunctional Nanomedicine with Silica: Role of Silica in Nanoparticles for Theranostic, Imaging, and Drug Monitoring. J. Colloid Interface Sci 2018, 521, 261–279. [PubMed: 29510868]

(7). Yoon YI; Pang X; Jung S; Zhang G; Kong M; Liu G; Chen X Smart Gold Nanoparticle-stabilized Ultrasound Micro-bubbles as Cancer Theranostics. J. Mater. Chem. B 2018, 6, 3235–3239. [PubMed: 30420913]

(8). Burkitt S; Mehraein M; Stanciauskas RK; Campbell J; Fraser S; Zavaleta C Label-Free Visualization and Tracking of Gold Nanoparticles in Vasculature Using Multiphoton Luminescence. Nanomaterials 2020, 10, 2239.

(9). Zeng S; Yong K-T; Roy I; Dinh X-Q; Yu X; Luan F A Review on Functionalized Gold Nanoparticles for Biosensing Applications. Plasmonics 2011, 6, 491–506.

(10). Mataji-Kojouri A; Ozen MO; Shahabadi M; Inci F; Demirci U Entangled Nanoplasmonic Cavities for Estimating Thickness of Surface-Adsorbed Layers. ACS Nano 2020, 14, 8518–8527. [PubMed: 32639713]

(11). Tokel O; Inci F; Demirci U Advances in Plasmonic Technologies for Point of Care Applications. Chem. Rev 2014, 114, 5728–5752. [PubMed: 24745365]

(12). Aldewachi H; Chalati T; Woodroofe MN; Bricklebank N; Sharrack B; Gardiner P Gold Nanoparticle-based Colorimetric Biosensors. Nanoscale 2018, 10, 18–33.

(13). Retout M; Valkenier H; Triffaux E; Doneux T; Bartik K; Bruylants G Rapid and Selective Detection of Proteins by Dual Trapping Using Gold Nanoparticles Functionalized with Peptide Aptamers. ACS Sens. 2016, 1, 929–933.

(14). Park J-E; Lee Y; Nam J-M Precisely Shaped, Uniformly Formed Gold Nanocubes with Ultrahigh Reproducibility in Single-particle Scattering and Surface-enhanced Raman Scattering. Nano Lett. 2018, 18, 6475–6482. [PubMed: 30153413]

(15). Barbosa S; Agrawal A; Rodríguez-Lorenzo L; Pastoriza-Santos I; Alvarez-Puebla RA; Kornowski A; Weller H; Liz-Marzán LM Tuning Size and Sensing Properties in Colloidal Gold Nanostars. Langmuir 2010, 26, 14943–14950. [PubMed: 20804155]

(16). Dreaden EC; Alkilany AM; Huang X; Murphy CJ; El-Sayed MA The Golden Age: Gold Nanoparticles for Biomedicine. Chem. Rev 2012, 41, 2740–2779.

(17). Lohse SE; Murphy CJ The Quest for Shape Control: A History of Gold Nanorod Synthesis. Chem. Mater 2013, 25, 1250–1261.

(18). Link S; Mohamed MB; El-Sayed MA Simulation of the Optical Absorption Spectra of Gold Nanorods as a Function of their Aspect Ratio and the Effect of the Medium Dielectric Constant. J. Phys. Chem. B 1999, 103, 3073–3077.

(19). Thakor AS; Jokerst J; Zavaleta C; Massoud TF; Gambhir SS Gold Nanoparticles: A Revival in Precious Metal Administration to Patients. Nano Lett. 2011, 11, 4029–4036. [PubMed: 21846107]

(20). Jin Z; Sugiyama Y; Zhang C; Palui G; Xin Y; Du L; Wang S; Dridi N; Mattoussi H Rapid Photoligation of Gold Nanocolloids with Lipoic Acid-Based Ligands. Chem. Mater 2020, 32, 7469–7483.

(21). Vigderman L; Khanal BP; Zubarev ER Functional Gold Nanorods: Synthesis, Self-assembly, and Sensing Applications. Adv. Mater 2012, 24, 4811–4841. [PubMed: 22740090]

(22). Pérez-Juste J; Pastoriza-Santos I; Liz-Marzán LM; Mulvaney P Gold Nanorods: Synthesis, Characterization and Applications. Colloidal Synth. Plasmonic Nanomet 2020, 15–88.

(23). Murphy CJ; Chang H-H; Falagan-Lotsch P; Gole MT; Hofmann DM; Hoang KNL; McClain SM; Meyer SM; Turner JG; Unnikrishnan M; Wu M; Zhang X; Zhang Y Virus-sized Gold Nanorods: Plasmonic Particles for Biology. Acc. Chem. Res 2019, 52, 2124–2135. [PubMed: 31373796]

(24). Vigderman L; Zubarev ER High-yield Synthesis of Gold Nanorods with Longitudinal SPR Peak Greater than 1200 nm Using Hydroquinone as a Reducing Agent. Chem. Mater 2013, 25, 1450–1457.

(25). Ye X; Jin L; Caglayan H; Chen J; Xing G; Zheng C; Doan-Nguyen V; Kang Y; Engheta N; Kagan CR; Murray CB Improved Size-tunable Synthesis of Monodisperse Gold Nanorods through the use of Aromatic Additives. ACS Nano 2012, 6, 2804–2817. [PubMed: 22376005]

(26). Soh JH; Lin Y; Thomas MR; Todorova N; Kallepitis C; Yarovsky I; Ying JY; Stevens MM Distinct Bimodal Roles of Aromatic Molecules in Controlling Gold Nanorod Growth for Biosensing. Adv. Mater 2017, 27, 1700523.

(27). Requejo KI; Liopo AV; Zubarev ER Gold Nanorod Synthesis with Small Thiolated Molecules. Langmuir 2020, 36, 3758–3769. [PubMed: 32216357]

(28). He M-Q; Chen S; Meng J; Shi W; Wang K; Yu Y-L; Wang J-H Capping Ligand Size-dependent LSPR Property Based on DNA Nanostructure-Mediated Morphological Evolution of Gold Nanorods for Ultrasensitive Visualization of Target DNA. Anal. Chem 2020, 92, 7054–7061. [PubMed: 32337976]

(29). Coronado-Puchau M; Saa L; Grzelczak M; Pavlov V; Liz-Marzán LM Enzymatic Modulation of Gold Nanorod Growth and Application to Nerve Gas Detection. Nano Today 2013, 8, 461–468.

(30). He M-Q; Chen S; Yao K; Meng J; Wang K; Yu Y-L; Wang J-H Precisely Tuning LSPR Property via “Peptide-Encoded” Morphological Evolution of Gold Nanorods for Quantitative Visualization of Enzyme Activity. Anal. Chem 2019, 92, 1395–1401. [PubMed: 31830782]

(31). Saa L; Coronado-Puchau M; Pavlov V; Liz-Marzán LM Enzymatic Etching of Gold Nanorods by Horseradish Peroxidase and Application to Blood Glucose Detection. Nanoscale 2014, 6, 7405–7409. [PubMed: 24874748]

(32). Rao H; Xue X; Wang H; Xue Z Gold Nanorod Etching-based Multicolorimetric Sensors: Strategies and Applications. J. Mater. Chem. C 2019, 7, 4610–4621.

(33). Liu Y; Lv B; Liu A; Liang G; Yin L; Pu Y; Wei W; Gou S; Liu S Multicolor Sensor for Organophosphorus Pesticides Determination Based on the Bi-enzyme Catalytic Etching of Gold Nanorods. Sens. Acuators B Chem 2018, 265, 675–681.

(34). Liu Y; Xu E; Xu C; Wei W Colorimetric Method for PARP-1 Detection Based on Preventing AuNRs from Etching by Molybdate. Sens. Acuators B Chem 2020, 325, 128806.

(35). Yang H; Liu A; Wei M; Liu Y; Lv B; Wei W; Zhang Y; Liu S Visual, Label-free Telomerase Activity Monitor via Enzymatic Etching of Gold Nanorods. Anal. Chem 2017, 89, 12094–12100. [PubMed: 29061046]

(36). Guo H; Song S; Dai T; Sun K; Zhou G; Li M; Mann S; Dou H Near-Infrared Fluorescent and Magnetic Resonance Dual-Imaging Coacervate Nanoprobes for Trypsin Mapping and Targeted Payload Delivery of Malignant Tumors. ACS Appl. Mater. Interfaces 2020, 12, 17302–17313. [PubMed: 32212678]

(37). Yang J; Gao Z; Ren X; Sheng J; Xu P; Chang C; Fu Y DeepDigest: Prediction of Protein Proteolytic Digestion with Deep Learning. Anal. Chem 2021, 93, 6094–6103. [PubMed: 33826301]

(38). Scarabelli L; Sánchez-Iglesias A; Pérez-Juste J; Liz-Marzán LMA “Tips and Tricks” Practical Guide to the Synthesis of Gold Nanorods. J. Phys. Chem. Lett 2015, DOI: 10.1021/acs.jpclett.5b02123.

(39). González-Rubio G; Kumar V; Llombart P; Díaz-Núñez P; Bladt E; Altantzis T; Bals S; Peña-Rodríguez O; Noya EG; MacDowell LG; Guerrero-Martínez A; Liz-Marzán LM Disconnecting Symmetry Breaking from Seeded Growth for the Reproducible Synthesis of High Quality Gold Nanorods. ACS Nano 2019, 13, 4424–4435. [PubMed: 30939242]

(40). Near RD; Hayden SC; Hunter RE Jr; Thackston D; El-Sayed MA Rapid and Efficient Prediction of Optical Extinction Coefficients for Gold Nanospheres and Gold Nanorods. J. Mater. Chem. C 2013, 117, 23950–23955.

(41). Jain PK; Lee KS; El-Sayed IH; El-Sayed MA Calculated Absorption and Scattering Properties of Gold Nanoparticles of Different Size, Shape, and Composition: Applications in Biological Imaging and Biomedicine. J. Phys. Chem. B 2006, 110, 7238–7248. [PubMed: 16599493]

(42). Park K; Drummy LF; Wadams RC; Koerner H; Nepal D; Fabris L; Vaia RA Growth Mechanism of Gold Nanorods. Chem. Mater 2013, 25, 555–563.

(43). Janicek BE; Hinman JG; Hinman JJ; Bae SH; Wu M; Turner J; Chang H-H; Park E; Lawless R; Suslick KS; Murphy CJ; Huang PY Quantitative Imaging of Organic Ligand Density on Anisotropic Inorganic Nanocrystals. Nano Lett. 2019, 19, 6308–6314. [PubMed: 31424951]

(44). Vigderman L; Manna P; Zubarev ER Quantitative Replacement of Cetyl Trimethylammonium Bromide by Cationic Thiol Ligands on the Surface of Gold Nanorods and their Extremely Large Uptake by Cancer Cells. Angew. Chem 2012, 124, 660–665.

(45). Hore MJA; Ye X; Ford J; Gao Y; Fei J; Wu Q; Rowan SJ; Composto RJ; Murray CB; Hammouda B Probing the Structure, Composition, and Spatial Distribution of Ligands on Gold Nanorods. Nano Lett. 2015, 15, 5730–5738. [PubMed: 26292087]

(46). Armbruster DA; Pry T Limit of Blank, Limit of Detection and Limit of Quantitation. Clin. Biochem. Rev 2008, 29, S49. [PubMed: 18852857]

(47). Nguyen DT; Kim D-J; Kim K-S Controlled Synthesis and Biomolecular Probe Application of Gold Nanoparticles. Micron 2011, 42, 207–227. [PubMed: 20952201]

(48). Park K; Hsiao M-S; Koerner H; Jawaid A; Che J; Vaia RA Optimizing Seed Aging for Single Crystal Gold Nanorod Growth: the Critical Role of Gold Nanocluster Crystal Structure. J. Mater. Chem. C 2016, 120, 28235–28245.

(49). Walsh MJ; Barrow SJ; Tong W; Funston AM; Etheridge J Symmetry Breaking and Silver in Gold Nanorod Growth. ACS Nano 2015, 9, 715–724. [PubMed: 25572634]

(50). Corbierre MK; Cameron NS; Lennox RB Polymer-stabilized Gold Nanoparticles with High Grafting Densities. Langmuir 2004, 20, 2867–2873. [PubMed: 15835165]

(51). Bieri M; Bürgi T L-Glutathione Chemisorption on Gold and Acid/base Induced Structural Changes: A PM-IRRAS and Time-resolved in situ ATR-IR Spectroscopic Study. Langmuir 2005, 21, 1354–1363. [PubMed: 15697281]

(52). Zhang J; Bilić A; Reimers JR; Hush NS; Ulstrup J Coexistence of Multiple Conformations in Cysteamine Monolayers on Au (111). J. Phys. Chem. B 2005, 109, 15355–15367. [PubMed: 16852948]

(53). Acres RG; Feyer V; Tsud N; Carlino E; Prince KC Mechanisms of Aggregation of Cysteine Functionalized Gold Nanoparticles. J. Phys. Chem. B 2014, 118, 10481–10487.

(54). Zweifel DA; Wei A Sulfide-arrested Growth of Gold Nanorods. Chem. Mater 2005, 17, 4256–4261. [PubMed: 17415410]

(55). Kou X; Zhang S; Yang Z; Tsung C-K; Stucky GD; Sun L; Wang J; Yan C Glutathione-and Cysteine-induced Transverse Overgrowth on Gold Nanorods. J. Am. Chem. Soc 2007, 129, 6402–6404. [PubMed: 17461586]

(56). Ha T; Ting AY; Liang J; Caldwell WB; Deniz AA; Chemla DS; Schultz PG; Weiss S Single-molecule Fluorescence Spectroscopy of Enzyme Conformational Dynamics and Cleavage Mechanism. Proc. Natl. Acad. Sci. U.S.A 1999, 96, 893–898. [PubMed: 9927664]

(57). Reinhard BM; Sheikholeslami S; Mastroianni A; Alivisatos AP; Liphardt J Use of Plasmon Coupling to Reveal the Dynamics of DNA Bending and Cleavage by Single EcoRV Restriction Enzymes. Proc. Natl. Acad. Sci. U.S.A 2007, 104, 2667–2672. [PubMed: 17307879]

(58). Dan K; Veetil AT; Chakraborty K; Krishnan Y DNA Nanodevices Map Enzymatic Activity in Organelles. Nat. Nanotechnol 2019, 14, 252–259. [PubMed: 30742135]

(59). Stenman U-H; Huhtala M-L; Koistinen R; Seppälä M Immunochemical Demonstration of an Ovarian Cancer-associated Urinary Peptide. Int. J. Cancer 1982, 30, 53–57. [PubMed: 6811446]

(60). Taccone W; Mazzon W; Belli M Evaluation of TATI and Other Markers in Solid Tumors. Scand. J. Clin. Lab. Invest 1991, 51, 25–32.

(61). Haglund C; Huhtala ML; Halila H; Nordling S; Roberts PJ; Scheinin TM; Stenman UH Tumour-associated Trypsin Inhibitor, TATI, in Patients with Pancreatic Cancer, Pancreatitis and Benign Biliary Diseases. Br. J. Cancer 1986, 54, 297–303. [PubMed: 3741764]

(62). Huhtala M-L; Kahanpää K; Seppää M; Halila H; Stenman U-H Excretion of a Tumor-associated Trypsin inhibitor (TATI) in Urine of Patients with Gynecological Malignancy. Int. J. Cancer 1983, 31, 711–714. [PubMed: 6190763]

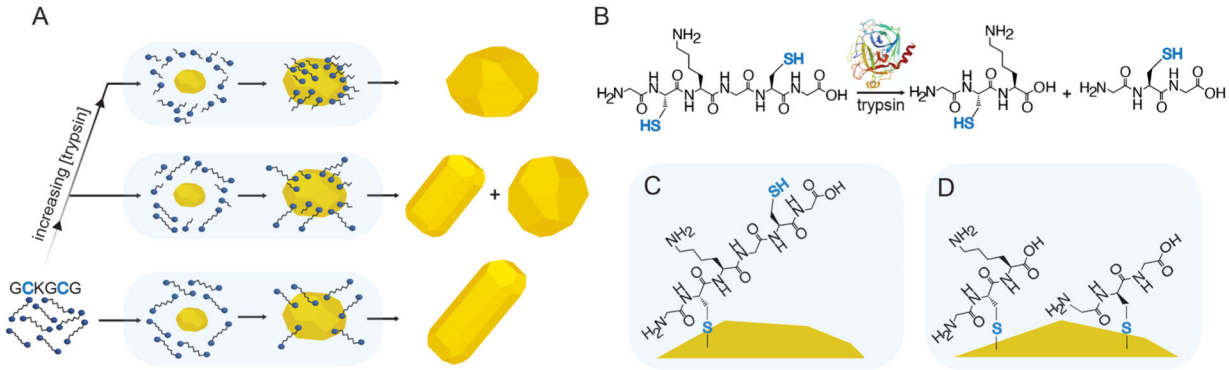

Figure 1.

Schematic of the sensing mechanism for the detection of trypsin. (A) Peptide-/protease-mediated gold nanoparticle growth and the effect of trypsin on the final nanoparticle morphology. The opaque blue background represents the growth solution. (B) Structure of the dithiol peptide GCKGCG and its subsequent cleavage by trypsin (PDB 1TRN) to produce two monothiol peptides, GCK and GCG. (C,D) Ligand-binding modes depicting the effective change in thiol concentration on the gold nanoparticle surface during growth without trypsin incubation (C) and with trypsin incubation (D).

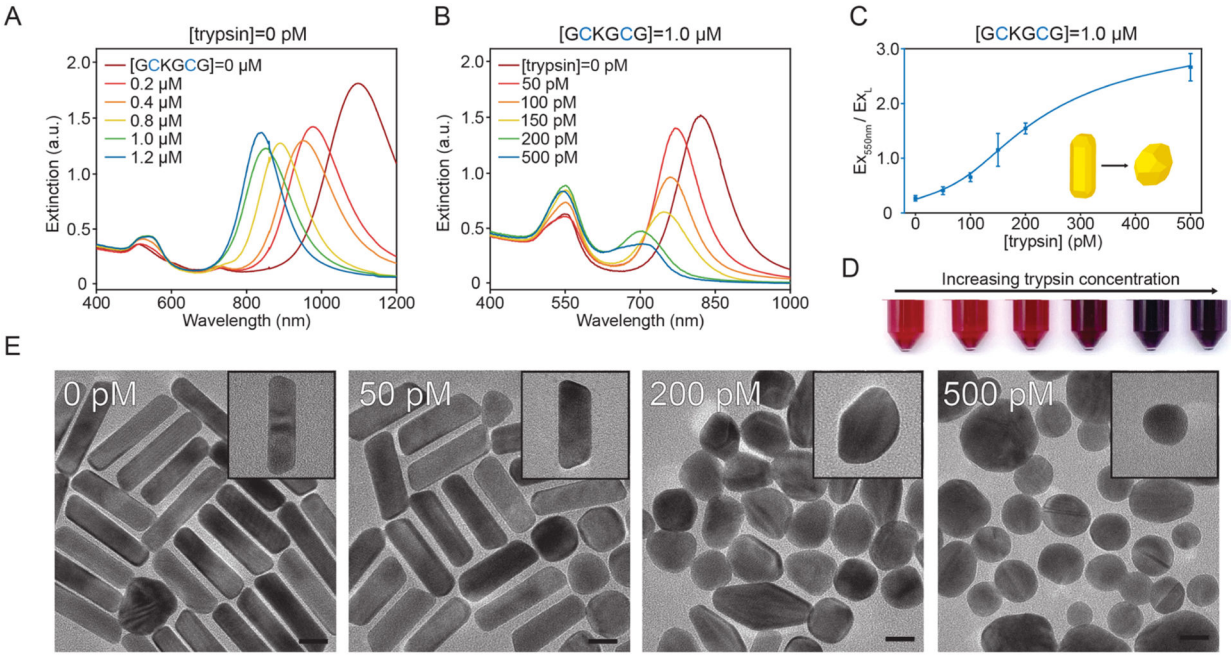

Figure 2.

Detection of trypsin. (A) Concentration-dependent UV–vis spectra of gold nanoparticles made with the protease substrate, GCKGCG. (B) Representative UV–vis spectra of gold nanoparticle samples made with a constant GCKGCG concentration and increasing trypsin concentration. (C) Increase in the ratio of Ex_{550nm} to Ex_L (longitudinal LSPR) as a function of trypsin concentration [limit of detection (LOD) = 45 pM, $n = 3$, error bars = SD, linear range 50–200 pM ($R^2 = 0.985$)]. (D) Image of nanoparticles prepared with 1.0 μM GCKGCG and increasing (left to right) trypsin concentration: 0, 50, 100, 150, 200, and 500 pM. (E) TEM images of nanoparticle samples grown in 1.0 μM GCKGCG and increasing trypsin concentration. Scale bars, 20 nm.

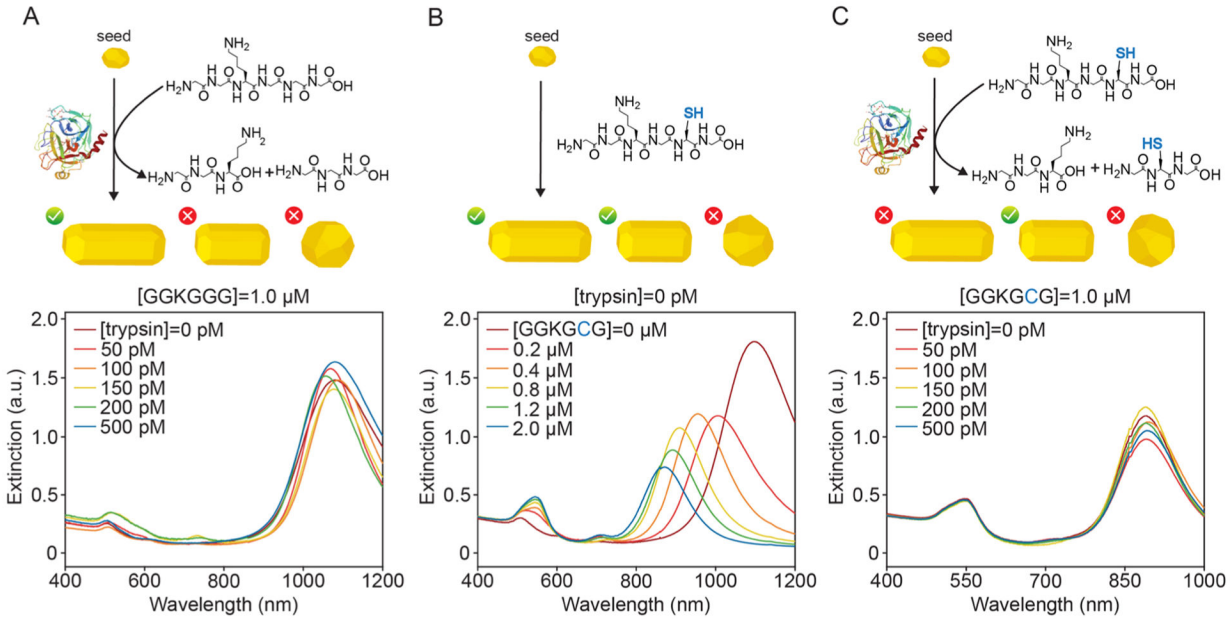

Figure 3.

Schematic of control peptides and the effect of thiol on AuNR growth. (A) Cleavage schematic and UV–vis spectra of nanoparticles prepared using the thiol-free peptide GGKGGG at a constant concentration and increasing trypsin concentration. AuNRs with an aspect ratio greater than 3.5 are synthesized; the growth process is unchanged in the presence of trypsin. (B) Schematic and concentration-dependent UV–vis spectra of gold nanoparticles made with the control monothiol peptide, GGKGCG. Increasing GGKGCG concentration results in a blue shift and a reduction in the aspect ratio of AuNRs. (C) Cleavage schematic and UV–vis spectra of gold nanoparticle samples prepared with a constant GGKGCG concentration and increasing trypsin concentration. AuNRs with an aspect ratio less than 3.5 are synthesized; the growth process is unchanged in the presence of trypsin.

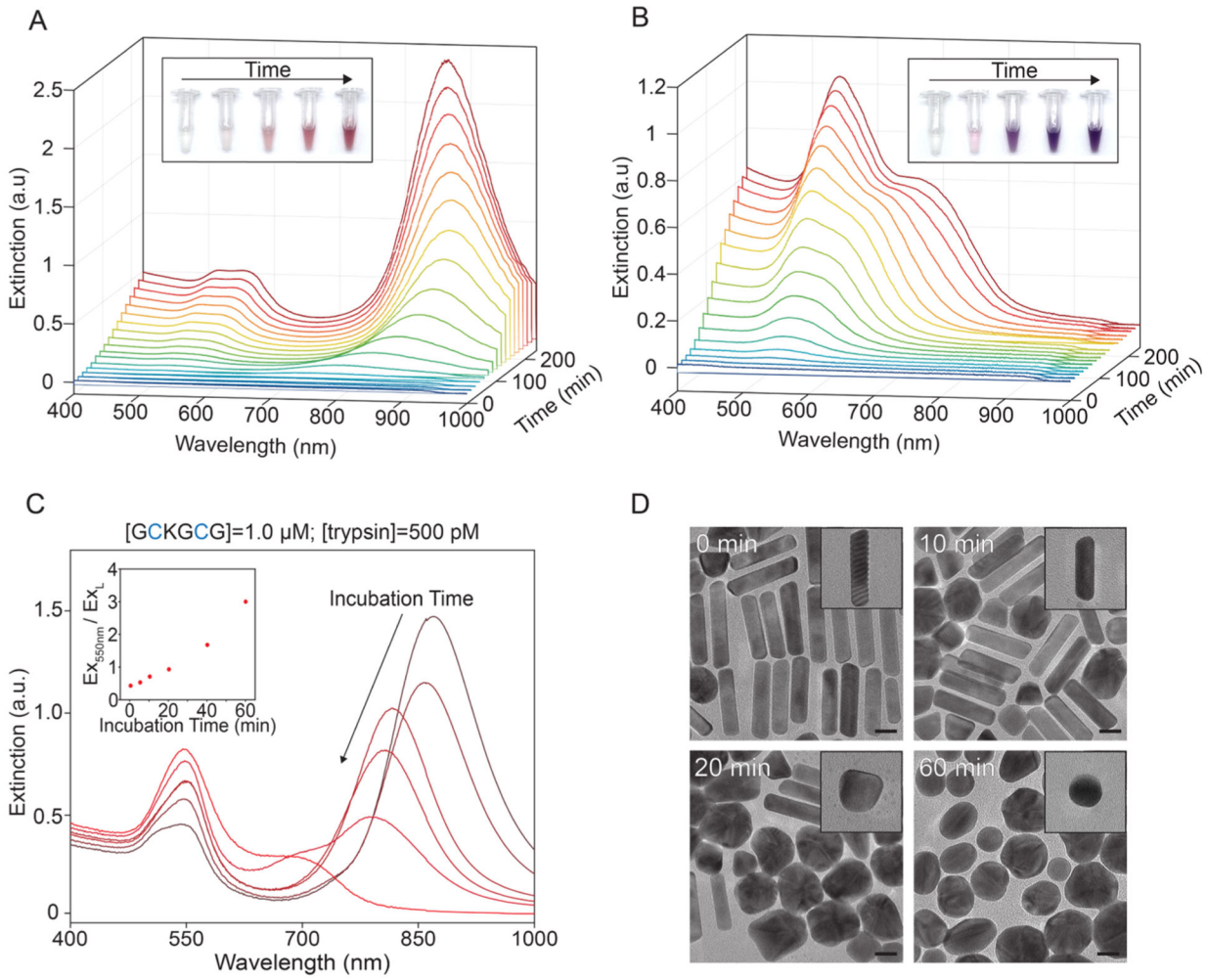

Figure 4.

Temporal study of proteolysis-modulated gold nanoparticle growth. (A,B) UV–vis spectra of gold nanoparticle time evolution with 15 min step size. Inset images were taken 0, 1, 2, 3, and 4 h after seed injection. (A) 1.0 μM GCKGCG and 0 pM trypsin. (B) 1.0 μM GCKGCG and 500 pM trypsin. (C, D) Incubation time-dependent detection of trypsin (Scheme S2). (C) UV–vis spectra of gold nanoparticles prepared with increasing incubation time prior to seed injection: 0, 5, 10, 20, 40, and 60 min. GCKGCG and trypsin concentration held constant. Inset: extinction ratio of Ex_{550nm} to Ex_L vs incubation time. (D) TEM images of nanoparticles prepared with 1.0 μM GCKGCG and 500 pM trypsin with incubation times of 0, 10, 20, and 60 min; scale bars: 20 nm.

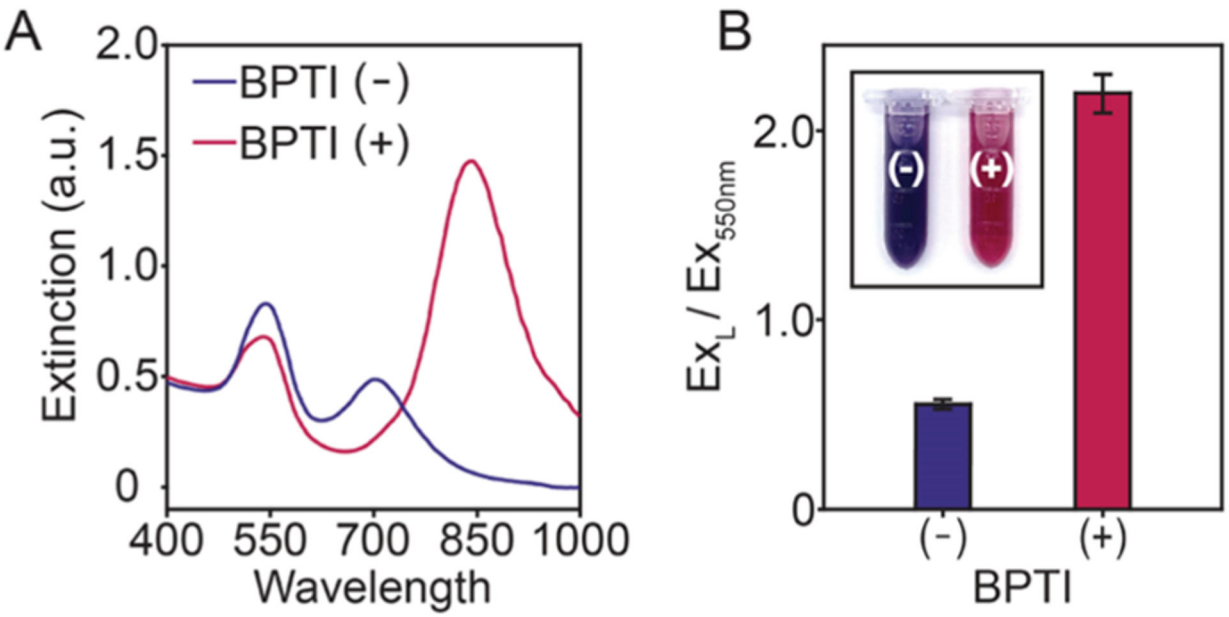

Figure 5.

Inhibition of trypsin with BPTI. Both samples were prepared with 1.0 μM GCKGCG and 500 pM trypsin. Experiments were performed in triplicate (n = 3, error bars = SD) with 0 nM BPTI (−) and 5 nM BPTI (+). (A) UV–vis spectra of nanoparticles prepared without (−) and with (+) BPTI. (B) Bar graph of the absorbance ratios of Ex_L and Ex_{550nm}.